

Formation and magnetic properties of spark plasma sintered $\text{Mn}_{3-\delta}\text{Ga}$ ($\delta = 0, 1$) alloys

Sonam Perween^{a,b}, A. Rathi^{a,b}, R. P. Singh^c, A. Bhattacharya^d, Parul Rani Raghuvanshi^d, P. V. Prakash Madduri^e, P. K. Rout^a, B. Sivaiah^{a,b}, Ajay Dhar^{a,b}, R. P. Pant^{a,b}, B. Gahtori^{a,b,†} and G. A. Basheed^{a,b,†}

^aCSIR-National Physical Laboratory (NPL), Dr. K. S. Krishnan Marg, New Delhi - 110012, India

^bAcademy of Scientific and Innovative Research (AcSIR), NPL Campus, New Delhi - 110012, India

^cDepartment of Physics, Indian Institute of Science Education and Research (IISER) Bhopal, Bhopal - 462023, India

^dDepartment of Metallurgical Engineering and Materials Science, IIT Bombay, Mumbai-400076, India

^eSchool of Physics, University of Hyderabad, Central University P. O., Hyderabad 500046, Telangana, India*

We present the synthesis of D0_{22} $\text{Mn}_{3-\delta}\text{Ga}$ ($\delta = 0, 1$) Heusler alloys by Spark Plasma Sintering method. The single phase Mn_3Ga ($T_c \simeq 780$ K) is synthesized, while Mn_2Ga ($T_c \simeq 710$ K) is found to coexist with a near-stoichiometric room temperature paramagnetic Mn_9Ga_5 ($\approx 15\%$) phase due to its lower formation energy, as confirmed from our density functional theory (DFT) calculations. The alloys show hard magnetic behavior with large room temperature spontaneous magnetization $m_s(80 \text{ kOe}) = 1.63$ (0.83) $\mu_B/\text{f.u.}$ and coercivity $H_c = 4.28$ (3.35) kOe for Mn_3Ga (Mn_2Ga). The magnetic properties are further investigated till T_c and the H_c (T) analysis by Stoner-Wohlfarth model shows the nucleation mechanism for the magnetization reversal. The experimental results are well supported by DFT calculations, which reveal that the ground state of D0_{22} Mn_2Ga is achieved by the removal of Mn-atoms from full Heusler Mn_3Ga structure in accordance with half Heusler alloy picture.

Keywords: Mn-based alloys, Heusler alloys, Coercivity mechanism, Density functional theory.

I. INTRODUCTION

The Mn-based Heusler alloys [1, 2] have gained extensive interest in magnetism research community because of their versatile magnetic behavior and consequent use in multi-functional applications, starting from spintronics to hard magnets. One such family is the $\text{Mn}_{3-\delta}\text{Ga}$ alloys in the tetragonal D0_{22} crystal structure [2–5] having a high Curie temperature ($T_c > 600$ K), large magnetic anisotropy $K_u \sim 10^6$ erg/cc and high spin polarization. Owing to these properties, the Mn-Ga family has emerged as a favorable system for hard magnets (in bulk [3, 4]) and spin-transfer-torque memory applications (in epitaxial thin films [5]). However, the synthesis of D0_{22} $\text{Mn}_{3-\delta}\text{Ga}$ ($0 \geq \delta \geq 1$) alloys has been a challenging task due to the existence of manifold stable near-stoichiometric and structural phases [6–8]. Till date, only arc melting technique has been used to synthesize bulk D0_{22} $\text{Mn}_{3-\delta}\text{Ga}$ ($\delta = 0, 1$) alloys [3, 4, 9–12], which show large discrepancies in the magnetic properties. Meanwhile, the magnetism in hard-magnetic alloys is largely controlled by the microstructure (grain size and homogeneity) of the sample [13, 14]. For better homogeneity, the arc-melting procedure needs to be repeated several times and further annealing for a long time (i.e. 1-2 weeks) is required [3, 4]. Besides, high evaporation rate of Mn makes it difficult for controlled and reliable synthesis of these alloys. Moreover, the preparation of a denser sputtering target requires hot-compression of arc-melted sample, which also leads to a much higher coercivity [15]. To avoid aforementioned issues, a better

alternative route to synthesize these alloys is single-step Spark Plasma Sintering (SPS) technique [16, 17]. In addition to quick sintering and annealing temperatures, the quasi-static compressive stress in SPS leads to maximum uniformity and high mechanical strength [18], which are highly advantageous for both hard magnets [19] and sputtering targets [17, 20].

The parent Mn_3Ga alloy is established as a full-Heusler alloy ($\text{XX}'\text{YZ}$) with a D0_{22} structure, which is a tetragonal variant of cubic L2_1 ($Fm\bar{3}m$) phase due to strong lattice distortion along c-axis [21]. This stabilizes $I4/mmm$ crystal symmetry, where two unique Mn (X/X' - 4d and Y - 2b) sites with an opposite arrangement of spins lead to a ferrimagnetic structure. In this picture, D0_{22} $\text{Mn}_{3-\delta}\text{Ga}$ ($0 \geq \delta \geq 1$) structure must be realized by creating Mn vacancies at 4d-site such that Mn_2Ga ($\delta = 1$) is a half-Heusler alloy (XYZ). However, the *ab initio* calculations [3] based on Heusler picture did not account the experimental results on D0_{22} $\text{Mn}_{3-\delta}\text{Ga}$ ($0 < \delta \leq 1$), and suggested the vacancy formation at both Mn sites. Moreover, the neutron diffraction studies on $\text{Mn}_{3-\delta}\text{Ga}$ thin film [22] and ribbons [23] suggest a substitution model with random site occupation of Mn (2b) and Ga (2a) atoms, which occurs for the tetragonal variant of B2-type structure [21]. Thus, the most intriguing issue is to identify the Mn-atoms (2b or 4d or both) that leave Mn_3Ga lattice to form a Mn_2Ga crystal structure and hence, to identify the ground state for Mn_2Ga .

Here, we synthesized the D0_{22} $\text{Mn}_{3-\delta}\text{Ga}$ ($\delta = 0, 1$) alloys using SPS technique for the first time. The magnetic properties of two alloys are investigated over wide temperature range (300 K to 950 K). We further employ density functional theory calculations to systematically study the formation and magnetic ground state of

*†basheedga@nplindia.org, bhasker@nplindia.org

$\text{Mn}_{3-\delta}\text{Ga}$ ($\delta = 0, 1$) alloys, which are found to be consistent with our experimental results.

II. EXPERIMENTAL DETAILS

The Mn_3Ga and Mn_2Ga alloys are synthesized by Spark Plasma Sintering (SPS Syntex, 725) method. The stoichiometric amount of high purity Mn (99.95%) and Ga (99.99%) are intermixed in glove box with an excess of 4 wt.% Mn to compensate the evaporation loss. The sintering is performed at 800 °C under a fixed pressure of 8.5 kN for Mn_3Ga with the heating and cooling rates of 100°C/min. A similar sintering process for Mn_2Ga is carried out at 800 °C under 6 kN pressure. The room temperature X-ray diffraction (XRD) patterns are recorded using Rigaku Miniflex diffractometer and analyzed with Rietveld method using FULLPROF program. The as-sintered Mn_3Ga shows mixed phase with hexagonal and D_{022} tetragonal structure whereas D_{022} tetragonal Mn_2Ga with $\approx 30\%$ of Mn_9Ga_5 phase is observed in as-sintered Mn_2Ga alloy. The differential scanning calorimetry (DSC) measurements are performed on as-sintered alloys to determine the annealing temperature for D_{022} phase formation. Following this, the sintered pellets are vacuum sealed in quartz tubes and annealed for 4 days at 725°C for Mn_3Ga and 400°C for Mn_2Ga with the heating and cooling rates of 10°C/min. The Energy-dispersive X-ray spectroscopy (EDS) measurements give an average stoichiometry of $\text{Mn}_{2.90(5)}\text{Ga}$ and $\text{Mn}_{2.05(5)}\text{Ga}$ for Mn_3Ga and Mn_2Ga samples, respectively. The detailed magnetic measurements are performed by physical properties measurement system (Quantum design) in the temperature range of 300 K to 950 K.

III. CALCULATIONAL DETAILS

The DFT calculations are carried out using VASP [24], a plane wave based electronic structure code with projected augmented wave potential [25]. Perdew-Burke-Ernzerhof (PBE) [26] exchange correlation functional within generalized gradient approximation (GGA) are employed. An energy cut off of 500 eV is used. The k-mesh is generated by Monkhorst-Pack method and the convergence of the results are tested by varying the mesh size. For the generation of the electronic density of states (DOS), denser k-grids are used. In all our calculations, self-consistency is achieved with numerical settings that yield a convergence for energy differences to $< 10^{-3}$ eV/atom. The atomic as well as geometrical optimization are performed via conjugate gradient minimization [27] and the forces on the atoms are converged to less than 0.001 eV/Å. The vibrational free energy of the compositions is calculated using phonopy [28].

IV. RESULT AND DISCUSSION

A. Structural Characterization

The room-temperature XRD patterns of SPS and vacuum annealed Mn_3Ga and Mn_2Ga alloys are shown in

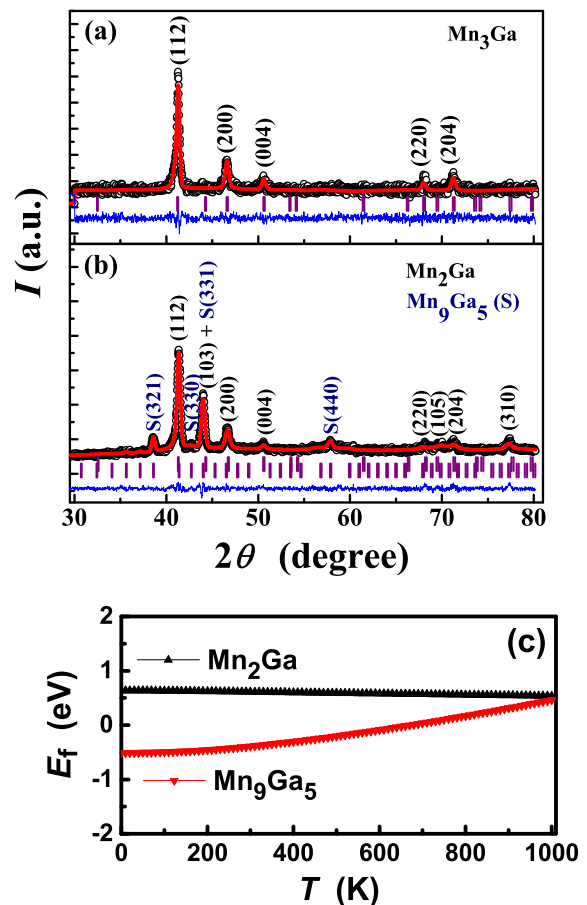


FIG. 1: Room temperature X-ray diffraction (XRD) patterns of (a) Mn_3Ga and (b) Mn_2Ga , fitted with single-phase $I4/mmm$ symmetry and two-phases i.e. main phase $I4/mmm$ and secondary phase(S) $P-43m$ symmetries, respectively using Rietveld method. (c) The thermal variation of the formation energy E_f for near-stoichiometric Mn_2Ga and Mn_9Ga_5 phases.

Fig. 1(a) and (b), respectively. The Rietveld refinement confirms the single tetragonal D_{022} phase (space group - $I4/mmm$) for Mn_3Ga with lattice parameters, $a = 3.897(1)$ Å and $c = 7.213(1)$ Å. On the other hand, the Mn_2Ga alloy is formed in tetragonal phase [$a = 3.890(1)$ Å, $c = 7.205(1)$ Å] with $\approx 15\%$ volume fraction of near-stoichiometric secondary Mn_9Ga_5 phase ($P-43m$ symmetry). In comparison to lattice parameters [$a = 3.904(5)$ Å, $c = 7.091(8)$ Å] for arc-melted Mn_3Ga [3, 29], the a for SPS Mn_3Ga is quite similar whereas c is notably larger. Furthermore, previous arc-melted studies show an increase of c parameter for Mn_2Ga compared to Mn_3Ga [3, 29]. In contrast, our SPS samples reveal a slight decrease of 'c' parameter from Mn_3Ga to Mn_2Ga , which is consistent with D_{022} Heusler alloy picture with partial removal of 4d Mn atoms from Mn_3Ga unit cell [21].

To understand the formation of secondary Mn_9Ga_5 phase during the synthesis of Mn_2Ga alloy, we performed DFT calculation of formation energy E_f for two compositions. Figure 1(c) shows the calculated E_f of Mn_2Ga

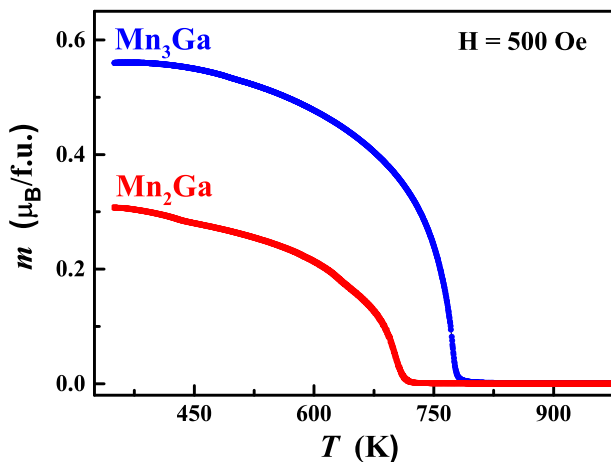


FIG. 2: The temperature dependence of dc magnetization for Mn_3Ga (blue) and Mn_2Ga (red) alloys in an applied magnetic field of 500 Oe.

and Mn_9Ga_5 with respect to bulk phases by including the contributions stemming from the vibrational free energy. The E_f for Mn_9Ga_5 comes out to be smaller than that of Mn_2Ga at the sintering temperature. This makes the exclusion of secondary Mn_9Ga_5 phase quite difficult during the synthesis of Mn_2Ga . Nevertheless, Mn_9Ga_5 ($T_c < 165$ K [30]) is non-magnetic in the temperature range (300-950 K) under study and thus do not contribute to the magnetic properties of Mn_2Ga .

B. Magnetic Characterization

Figure 2 shows the temperature dependence of dc magnetization, $m(T)$ for Mn_3Ga and Mn_2Ga . The $m(T)$ show a sharp increase below $T_c \simeq 780$ K and $\simeq 710$ K for Mn_3Ga and Mn_2Ga , respectively, which is consistent with previous arc-melting study [3]. Complementary XRD study, the $m(T)$ results unambiguously confirm the successful synthesis of D_{022} $\text{Mn}_{3-\delta}\text{Ga}$ alloys.

The field dependent magnetization, $m(H)$ loops for Mn_3Ga and Mn_2Ga at selected temperatures are depicted in Fig. 3. The $m(H)$ loops exhibit a broad hysteresis with non-saturating behavior up to 80 kOe, which can be associated with a ferrimagnetic structure and strong magnetic anisotropy present in these hard magnetic alloys. The room temperature spontaneous magnetization (m_s) is observed to be $1.63 \mu_B$ at 80 kOe ($1.45 \mu_B$ at 50 kOe) for Mn_3Ga , which is significantly larger than $\sim 1.1 \mu_B$ (at 50 kOe) reported for arc melted alloy [3, 31]. This may be attributed to significantly larger 'c' parameter in SPS Mn_3Ga , as Mn-Mn exchange coupling increases with interatomic distance [32]. In comparison, the room temperature m_s for Mn_2Ga is $0.83 \mu_B$ at 80 kOe, which is nearly half of the Mn_3Ga value. This is directly linked to the structural evolution from Mn_3Ga to Mn_2Ga with the formation of Mn-vacancies (either at 4d or 2b or both the sites). Moreover, on increasing the temperature, the m_s decreases in a typical Bloch's law manner [33], which confirms the long-range ferrimagnetic ordering in these

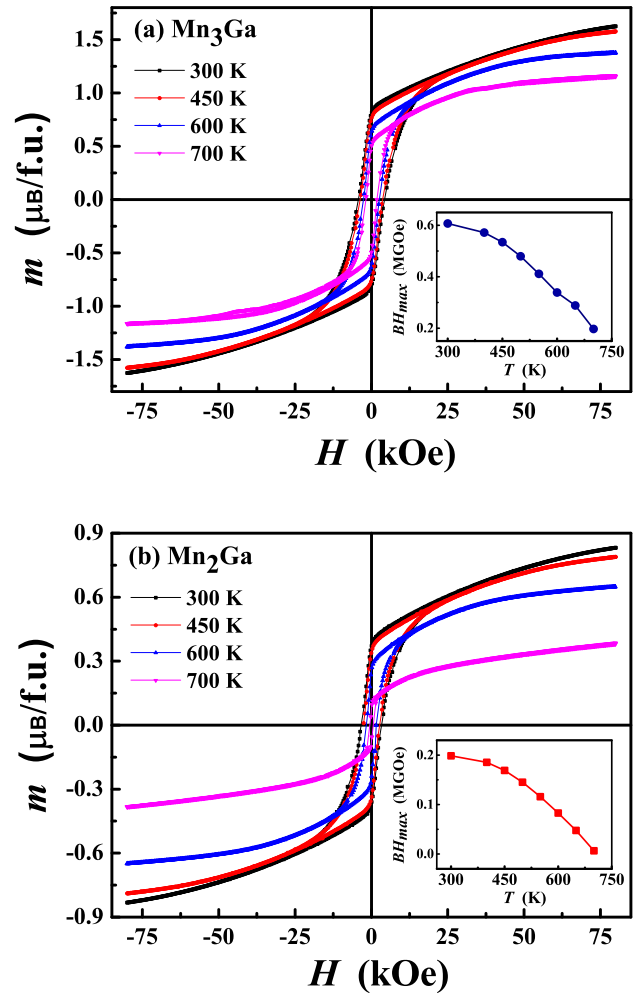


FIG. 3: The field dependant magnetization curves of (a) Mn_2Ga and (b) Mn_3Ga for selected temperatures. The inset shows the thermal variation of maximum energy product (BH_{max}).

alloys. Here, we want to point out that in contrast to present SPS study, the previous arc-melting study [3] shows a increase of moment from Mn_3Ga to Mn_2Ga , which has been modeled by an *ab initio* study with removal of Mn-atoms from both the Mn-sites (one-third from 4d-site and two-third from 2b-site). Such contrasting behavior may stem from the difference in growth techniques. Unlike the formation of alloys “freely” in “arc-melting” technique, the “SPS” method involves large quasi-static compressive stress, which can result in different atomic arrangement within the unit cell, in particular for partially-filled structures like Mn_2Ga . This issue is further analyzed using DFT calculations in section 4.3.

We now turn to the hard magnetic behavior in two alloys. The $m(H)$ loops also shows a large room temperature coercivity (H_c) of 4.29 kOe (3.35 kOe) for Mn_3Ga (Mn_2Ga), which monotonically decreases with temperature [See Fig. 4]. The hardening of magnetic materials is generally dependent on the magnetic anisotropy in the system, which acts against the coherent rotation of

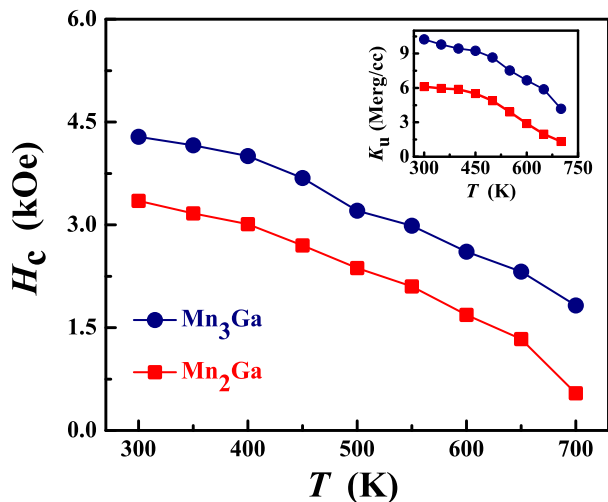


FIG. 4: The temperature dependence of coercivity (H_c) for Mn_3Ga (blue circles) and Mn_2Ga (red squares). The inset shows the temperature dependent uniaxial magneto-crystalline anisotropy (K_u) extracted from ATS analysis with respective color coding.

the magnetic moments, according to Stoner-Wohlfarth model [34]. We have estimated the effective magnetic anisotropy by fitting $m(H)$ isotherms to the law of “*approach to saturation*” (ATS) [35, 36] given as: $m(T, H) = \chi_{hf} \times H + m_{sat}[1 - b(T)/H^2]$. Here, χ_{hf} represents high field susceptibility due to paraprocesses and the coefficient $b(T)$ relates to the magnetic anisotropy in the system. The nature of magnetic anisotropy can be qualitatively determined from the remanence ratio (m_r/m_s), which is found to be ~ 0.49 (0.44) for Mn_3Ga (Mn_2Ga) alloy. The m_r/m_s values for two alloys are very close to 0.5 as expected for uniaxial anisotropy. This indicates the presence of uniaxial magneto-crystalline anisotropy (K_u) for two alloys. In that case, $b(T)$ is related to $K_u(T)$ by the relation, $b(T) = 4 K_u^2(T)/15 m_{sat}^2(T)$ [36].

We have fitted the $m(H)$ isotherms at all the temperatures with “*ATS model*” for $H \geq 50$ kOe and determined the temperature dependence of K_u , as shown in the inset of Fig. 4. The room temperature K_u values are 10.24 Merg/cc and 6.11 Merg/cc for Mn_3Ga and Mn_2Ga , respectively. The $K_u(T)$ can be related to $H_c(T)$ through modified Stoner-Wohlfarth (SW) relation [14, 37], $H_c(T) = \alpha(T) \times 2K_u(T)/m_{sat}(T)$, where $\alpha(T)$ is the microstructural parameter ($\alpha = 1$ for ideal uniform magnetization reversal against the anisotropy). The domain wall movement resulting from the nucleation (with respect to initial magnetic state) or pinning of magnetic domains in inhomogeneous regions reduces the anisotropy by the factor $\alpha(T)$. The two mechanism can be distinguished by α -parameter, which is > 0.3 for nucleation process, whereas < 0.3 for combined pinning and nucleation processes [14]. Our $H_c(T)$ analysis using modified SW model gives $\alpha(T) \sim 0.7$ (Mn_3Ga) and 0.5 (Mn_2Ga) up to T_c . The $\alpha(T)$ values (> 0.3) suggest that the nucleation process is mainly responsible for hardening

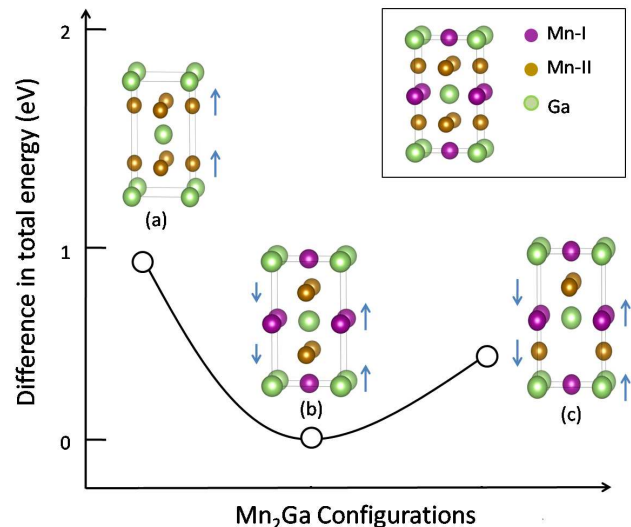


FIG. 5: The calculated total energy difference (per formula unit) of various Mn_2Ga configurations (a,b,c) with respect to its minimum energy ground state (b), along with the arrangement of magnetic moments at two (Mn-I and Mn-II) sites. The unit cell for Mn_3Ga is shown in the inset.

of these two alloys. Moreover, the comparatively lower $\alpha(T)$ from Mn_2Ga may result from presence of partial Mn-vacancies (defects) in distorted ferrimagnetic structure of Mn_2Ga . We have also calculated the characteristic parameter for hard magnet viz. maximum energy product, $BH_{max} = Max(-B \times H)$ in second quadrant. The room temperature BH_{max} values at 80 kOe are 0.61 MGOe and 0.2 MGOe for Mn_3Ga and Mn_2Ga , respectively. The thermal variation of BH_{max} for two alloys is shown in inset of Fig. 3, which show a similar behavior to $H_c(T)$. Here, we point out that the large discrepancy has been observed in previously reported room temperature magnetic properties like m_s , H_c and BH_{max} for arc-melted alloys [3, 4, 9–12]. To understand the differences in our results from previously reported arc-melted studies, the evolution of chemical and magnetic structure from Mn_3Ga to Mn_2Ga has been further investigated using DFT calculations.

C. Magnetic Ground state: DFT Calculations

To determine the minimum energy ground state for DO_{22} Mn_3Ga and Mn_2Ga alloys, we have carried out DFT calculations by taking unit cell dimension of experimentally determined lattice parameters. In DO_{22} -type Mn_3Ga unit cell with $I4/mmm$ symmetry, Mn-atoms occupy two different Mn-sites, namely, Mn-I at 2b (0, 0, 1/2) and Mn-II at 4d (0, 1/2, 1/4) wyckoff positions with a multiplicity of 1 and 2, respectively, while Ga atoms only occupy 2a site [see inset of Fig. 5]. This is in consistent with Heusler alloy picture [21]. In this structure, the magnetic moments at Mn-I (2b) and Mn-II (4d) sites have antiparallel arrangement, leading to a ferrimagnetic

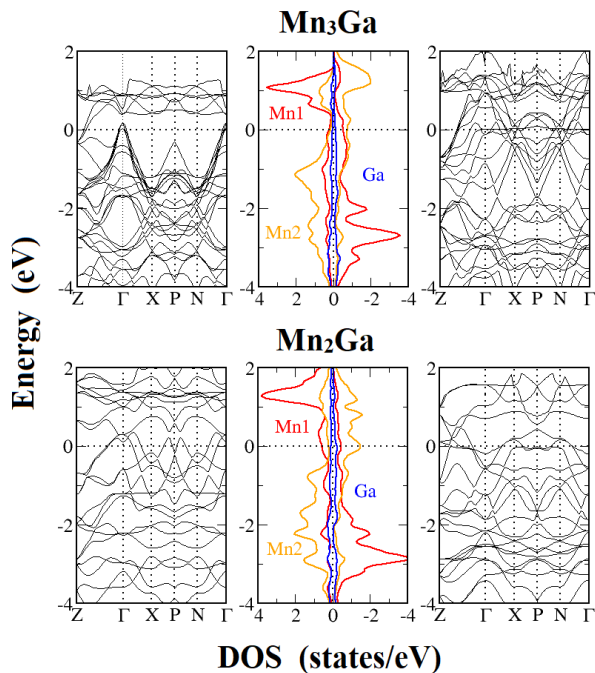


FIG. 6: The atom projected (color coded) density of states (middle panel) and the spin up (left panel) and spin down (right panel) band structure of Mn-Ga alloys. The Fermi level is set at ‘zero’.

structure. Next, the $\text{Mn}_{3-\delta}\text{Ga}$ ($\delta \neq 0$) unit cell can be realized by removal of Mn from Mn_3Ga unit cell at either (i) Mn-I site, or (ii) Mn-II site or (iii) both Mn-I and Mn-II sites. Here, we study the minimum energy ground state of Mn_2Ga ($\delta = 1$) by unraveling several structural configurations. In Fig. 5, the total energy difference of three main partially filled D_{022} -type Mn_2Ga configurations with respect to lowest energy configuration is plotted. The complete removal of Mn-I (2b) atoms [cf. configuration (a)] results in a high energy configuration with ferromagnetic alignment of magnetic moments at Mn-II (4d) sites ($P4/mmm$ symmetry). In comparison, the removal of Mn-atoms only from Mn-II (4d) sites results in lower energy [cf. configurations (b) and (c)], leading to a $I4/mmm$ symmetry for Mn_2Ga also; this is in consistent with half-Heusler alloy structure [21]. Out of several such possibilities, the configuration (b) in Fig. 5 represents the minimum energy (ground) state for D_{022} Mn_2Ga with $I4/mmm$ symmetry.

The magnetic moments associated with D_{022} -type Mn_3Ga and Mn_2Ga ground states have been extracted from the total and atom projected density of states (DOS) calculations [see Fig. 6]. In all cases, the Mn atoms mainly contribute to the magnetic moment in these compounds, as evident from the prominent split in the spin up (\uparrow) and spin down (\downarrow) contribution of the Mn atoms in the DOS near the Fermi level. The symmetrically inequivalent Mn atoms at 2b and 4d sites lead to

different (opposite) magnetic contributions. In Mn_3Ga configuration, the net atomic magnetic moments (m_s) of

System	Atomic Moments in μ_B			Total moment in $\mu_B/\text{f.u.}$	
	(Multiplicity)			W/O SOC	W SOC
	Mn-I	Mn-II	Ga		
Mn_3Ga	-2.841(1)	2.307(2)	-0.065(1)	1.74	1.8
Mn_2Ga	-3.207(1)	1.837(2)	-0.010(1)	1.39	1.46

TABLE I: The atom specific and net magnetic moments per f.u. with (W) and without (W/O) spin orbit coupling (SOC), and spin polarization of Mn_3Ga and Mn_2Ga alloys.

2.841 μ_B at Mn-I (2b) and 2.307 μ_B at Mn-II (4d) sites lead to an effective magnetic moment, $m = 2 m_{II} - m_I - m_{Ga} = 1.74 \mu_B/\text{f.u.}$ for the system. Whereas, with the removal of a Mn-II (4d) atoms in Mn_2Ga unit cell, the (effective) major contribution comes from Mn-I (2b) site (3.207 μ_B) in comparison to Mn-II (4d) site (1.837 μ_B), resulting in a net magnetic moment, $m = m_I - m_{II} + m_{Ga} = 1.39 \mu_B/\text{f.u.}$ for Mn_2Ga . The inclusion of spin-orbit coupling (SOC) leads to a small increment in net magnetic moment for two alloys. Furthermore, the spin polarization for two alloys is calculated as 58% (53%) for Mn_3Ga (Mn_2Ga), which is in agreement with the experimental study [5]. The summarized atom specific and net magnetic moments in Mn_3Ga and Mn_2Ga alloys without (W/O) and with (W) SOC along with spin polarization are enlisted in Table I. Thus, the DFT calculations clearly shows that Mn_2Ga adopts a half Heusler structure with removal of only Mn-II (4d) atoms from full Heusler Mn_3Ga unit cell, leading to a significant decrease in net magnetic moment in comparison to Mn_3Ga . This supports our experimental results on SPS D_{022} $\text{Mn}_{3-\delta}\text{Ga}$ ($\delta = 0, 1$) alloys.

V. CONCLUSION

In summary, we synthesized the $\text{Mn}_{3-\delta}\text{Ga}$ ($\delta = 0, 1$) alloys with D_{022} tetragonal structure by Spark Plasma sintering technique. The magnetization measurements reveal $T_c \simeq 780$ K and $\simeq 710$ K for Mn_3Ga and Mn_2Ga , respectively. The magnetic hysteresis loops for Mn_3Ga (Mn_2Ga) yield large room temperature spontaneous magnetization m_s of 1.63 (0.83) $\mu_B/\text{f.u.}$ at 80 kOe, BH_{max} of 0.61 (0.20) MGOe as well as coercivity, H_c of 4.285 (3.35) kOe. The Stoner-Wohlfarth model reveals that the magnetic reversal in these alloys are dominated by nucleation mechanism. Furthermore, we employ DFT calculations to identify the ground state structures and the associated magnetic properties of D_{022} $\text{Mn}_{3-\delta}\text{Ga}$ ($\delta = 0, 1$) alloys, which are in support of our experimental results. Finally, we point out that the SPS technique offers a controlled synthesis of D_{022} $\text{Mn}_{3-\delta}\text{Ga}$ ($0 \geq \delta \geq 1$) alloys, preserving the Heusler alloy structure.

-
- [1] L. Wollmann, S. Chadov, J. Kübler, and C. Felser, *Phys. Rev. B* **90**, 214420 (2014).
- [2] L. Wollmann, S. Chadov, J. Kübler, and C. Felser, *Phys. Rev. B* **92**, 064417 (2015).
- [3] J. Winterlik, B. Balke, G. H. Fecher, C. Felser, M. C. M. Alves, F. Bernardi, and J. Morais, *Phys. Rev. B* **77**, 054406 (2008).
- [4] H. Niida, T. Hori, H. Onodera, Y. Yamaguchi, and Y. Nakagawa, *J. Appl. Phys.* **79**, 5946 (1996).
- [5] H. Kurt, K. Rode, M. Venkatesan, P. Stamenov, and J. M. D. Coey, *Phys. Stat. Solid. B* **248**, 2338 (2011).
- [6] H. G. Meissner, K. Schubert, and T. R. Anantharaman, *Proc. of the Indian Academy of Sciences - Section A* **61**, 340 (1965).
- [7] X. S. Lu, J. K. Liang, T. J. Shi, and M. G. Zhou, *Acta Phys. Sin.* **29**, 469 (1980).
- [8] K. Minakuchi, R. Y. Umetsu, K. Ishida, and R. Kainuma, *J. Alloys Compd.* **537**, 332 (2012).
- [9] Q. M. Lu and M. Yu, *Sci. Rep.* **5**, 17086 (2015).
- [10] T. Saito and R. Nishimura, *J. Appl. Phys.* **112**, 083901 (2012).
- [11] S. Perween, A. Rath, P. Babu, G. Gupta, B. Sivaiah, R. P. Pant, B. Gahtori, and G. A. Basheed, *J. Magn. Magn. Mater.* **473**, 278 (2019).
- [12] R. Rejali, D. H. Ryan, Z. Altounian, C. Boyer, Q. Lu, M. Wang, H. Zhang, and M. Yue, *AIP Adv.* **6**, 056003 (2016).
- [13] J. D. Livingston, *J. Appl. Phys.* **52**, 2544 (1981).
- [14] *J. Magn. Magn. Mater.* **74**, 291 (1988).
- [15] T. Mix, K.-H. Mller, L. Schultz, and T. Woodcock, *J. Magn. Magn. Mater.* **391**, 89 (2015).
- [16] O. Guillon, J. Gonzalez-Julian, B. Dargatz, T. Kessel, G. Schierning, J. Rthel, and M. Herrmann, *Adv. Engg. Mater.* **16**, 830 (2014).
- [17] M. Tokita, in *Handbook of Advanced Ceramics* (Academic Press, Oxford, 2013), pp. 1149 – 1177, 2nd ed.
- [18] Z. A. Munir, U. Anselmi-Tamburini, and M. Ohyanagi, *J. Mater. Sci.* **41**, 763 (2006).
- [19] W. Mo, L. Zhang, A. Shan, L. Cao, J. Wu, and M. Komuro, *Intermetallics* **15**, 1483 (2007).
- [20] M. V. Lungu, E. Enescu, D. Tălpeanu, D. Pătroi, V. Marinescu, A. Sobetkii, N. Stancu, M. Lucaci, M. Marin, and E. Manta, *Mater. Research Express* **6**, 076565 (2019).
- [21] T. Graf, C. Felser, and S. S. Parkin, *Prog. Solid State Chem.* **39**, 1 (2011).
- [22] S. Mizukami, T. Kubota, F. Wu, X. Zhang, T. Miyazaki, H. Naganuma, M. Oogane, A. Sakuma, and Y. Ando, *Phys. Rev. B* **85**, 014416 (2012).
- [23] H. Zhao, W. Yang, Z. Shao, G. Tian, D. Zhou, H. Du, S. Liu, J. Han, C. Wang, J. Xu, et al., *Scripta Mater.* **129**, 6 (2017).
- [24] G. Kresse and J. Hafner, *Phys. Rev. B* **49**, 14251 (1994).
- [25] P. E. Blöchl, *Phys. Rev. B* **50**, 17953 (1994).
- [26] J. P. Perdew, K. Burke, and M. Ernzerhof, *Phys. Rev. Lett.* **78**, 1396 (1997).
- [27] P. Pulay, *Chem. Phys. Lett.* **73**, 393 (1980).
- [28] A. Togo and I. Tanaka, *Scripta Mater.* **108**, 1 (2015).
- [29] J. Z. Wei, R. Wu, Y. B. Yang, X. G. Chen, Y. H. Xia, Y. C. Yang, C. S. Wang, and J. B. Yang, *J. Appl. Phys.* **115**, 17A736 (2014).
- [30] P. Tozman, J. Coey, and Z. GerCSI, *Acta Mater.* **113**, 147 (2016).
- [31] B. Balke, G. H. Fecher, J. Winterlik, and C. Felser, *Appl. Phys. Lett.* **90**, 152504 (2007).
- [32] N. Yamada, *J. Phys. Society of Japan* **59**, 273 (1990).
- [33] S. Cojocaru, A. Naddeo, and R. Citro, *EPL (Europhysics Lett.)* **106**, 17001 (2014).
- [34] E. C. Stoner and E. P. Wohlfarth, *Philosophical Transactions of the Royal Society of London A: Mathematical, Physical and Engineering Sciences* **240**, 599 (1948).
- [35] S. N. Kaul and U. Messala, *J. Magn. Magn. Mater.* **401**, 539 (2016).
- [36] A. Rath, P. Babu, P. Rout, V. Awana, V. K. Tripathi, R. Nagarajan, B. Sivaiah, R. P. Pant, and G. A. Basheed, *J. Magn. Magn. Mater.* **474**, 585 (2019).
- [37] D. Givord, Q. Lu, M. Rossignol, P. Tenaud, and T. Viadieu, *J. Magn. Magn. Mater.* **83**, 183 (1990).